Journal of Power Sources 188 (2009) 82–88

Contents lists available at ScienceDirect

Journal of Power Sources

journal homepage: www.elsevier.com/locate/jpowsour

Dry gas operation of proton exchange membrane fuel cells with parallel channels: Non-porous versus porous plates

Shawn Litster[1], Juan G. Santiago*

Dept. of Mechanical Engineering, Stanford University, Stanford, CA 94305, USA

ARTICLE INFO

Article history:
Received 7 October 2008
Received in revised form
13 November 2008
Accepted 14 November 2008
Available online 27 November 2008

Keywords:
PEM fuel cell
Water management
Porous plate
Wick
Heat pipe
Dry gas

ABSTRACT

We present a study of proton exchange membrane (PEM) fuel cells with parallel channel flow fields for the cathode, dry inlet gases, and ambient pressure at the outlets. The study compares the performance of two designs: a standard, non-porous graphite cathode plate design and a porous hydrophilic carbon plate version. The experimental study of the non-porous plate is a control case and highlights the significant challenges of operation with dry gases and non-porous, parallel channel cathodes. These challenges include significant transients in power density and severe performance loss due to flooding and electrolyte dry-out. Our experimental study shows that the porous plate yields significant improvements in performance and robustness of operation. We hypothesize that the porous plate distributes water throughout the cell area by capillary action; including pumping water upstream to normally dry inlet regions. The porous plate reduces membrane resistance and air pressure drop. Further, IR-free polarization curves confirm operation free of flooding. With an air stoichiometric ratio of 1.3, we obtain a maximum power density of 0.40 W cm^{-2}, which is 3.5 times greater than that achieved with the non-porous plate at the same operating condition.

1. Introduction

Commercialization of PEM fuel cell technology faces significant hurdles in terms of cost, durability, and reliability. Technological advancements are necessary for the development of robust, economical fuel cell systems with high power densities, low parasitic loads, and minimal ancillary components [1]. For example, the power for air delivery is the largest parasitic load on automotive fuel cell systems [2] and significant volume is afforded to gas conditioning equipment in existing automotive systems. Implementations of ambient pressure air, parallel channel flow fields, or near-stoichiometric flow rates are all viable means of reducing the air delivery parasitic load. Miniature fuel cell stacks for portable power [3–6] often feature open ended parallel channels [7] or post-type [3] cathode flow fields that allow for low-pressure ambient air delivery by natural convection or forced convection with fans. However, parallel channel cathode architectures and low air flow rates typically lead to flooding of the fuel cell [8,9].

PEM fuel cells with perfluorosulfonic acid (PFSA) membranes, such as Nafion, require high levels of humidity for adequate ionic conductivity [10]. Gas flow in the cathode channels normally advects product water downstream towards the outlet; and so systems often recuperate water from the exhaust gases and transfer it to the incoming gas streams for humidification. Water recuperation and humidification of the gases are achieved with condensers, water separators, and heat and humidification exchangers integrated into the balance of plant [11]. In fuel cells for portable power applications, the volume and system complexity introduced by these humidification components can be prohibitive and such fuel cells often operate passively without water recuperation [12]. Operation of PEM fuel cells with dry gases offers a means to reduce system cost, complexity, weight, and size by eliminating the water management components. Operation with dry inlet gases, however, can be difficult as this promotes severe membrane dry-out [12].

There are several approaches to internally recirculate water for humidification without external gas conditioning components. Perhaps the least invasive approach is routing hydrogen and air flows in a counter-flow fashion such that gases are hydrated by transmembrane water transport [13]. A similar approach is the double-path-type anode flow field described by Qi and Kaufman [14], which uses adjacent hydrogen channels flowing in opposing directions for moisture exchange. More invasive approaches involve integrating wicking components into the fuel cell. Prior work on integrating wicks includes Watanabe et al.'s [15] integration of

* Corresponding author at: Building 530, Room 225, 440 Escondido Mall, Stanford, CA 94305, USA. Tel.: +1 650 723 5689; fax: +1 650 723 7657.
E-mail addresses: litster@andrew.cmu.edu (S. Litster), juan.santiago@stanford.edu (J.G. Santiago).
[1] Present address: Dept. of Mechanical Engineering, Carnegie Mellon University, Pittsburgh, PA 15213, USA.

0378-7753/$ – see front matter © 2008 Elsevier B.V. All rights reserved.
doi:10.1016/j.jpowsour.2008.11.069

Nomenclature

F	Faraday's constant
I	current
j_{FC}	current density
M_{H_2O}	molar mass of water
$\dot{m}$	mass flow rate
Δp	pressure drop
R_{mem}	specific membrane resistance
T	temperature
V_{FC}	voltage

Greek symbols

α	stoichiometric ratio
β	water content
φ	relative humidity

Subscripts and superscripts

an	anode
ca	cathode
in	inlet
out	outlet

porous strands into membranes for humidification, United Technologies Corporation's porous water transport plates [16,17], Ge et al.'s [18,19] isolated wicks within flow fields, and our group's prior work on coupling integrated wicks with external electroosmotic (EO) pumps for active water removal [9,20]. Of these prior published studies on using wicks, the fuel cell of Ge et al. is the only passive system that does not have additional components, such as pumps, to apply pressure on the liquid water within the wick. Their system featured two strips of wick laid over the turns of the serpentine channels along the sides of the active area. They demonstrated with polarization curves that the wicks significantly improve performance by passively humidifying the gases. However, there was no evidence that their wick system addressed flooding or that flooding occurred in their fuel cell without wicks. The lack of flooding symptoms is likely due to their serpentine flow field design. In addition, the majority of their studies were performed at elevated gas pressures (300 kPa) and a moderate air stoichiometric ratio of 2.

We here present a study of the performance of a PEM fuel cell with integrated porous carbon wicks for both flood prevention and internal humidification of dry, ambient pressure gases within a parallel channel flow field. Fig. 1 illustrates our hypothesis for the water transport mechanism for passive humidification of the air in a porous hydrophilic plate. The fuel cell produces water along the entire length of the fuel cell channel because of the oxygen reduction reaction. For sufficiently low air stoichiometric ratios, the air becomes vapor saturated at downstream locations where water is produced as liquid. Liquid water is wicked by the porous plate and capillary forces drive liquid water towards the inlet. As water travels upstream, it passively humidifies the air via convective mass transfer (evaporation). Thus, the porous plate provides a passive humidification mechanism that internally recuperates and recirculates water. This water recirculation mechanism is analogous to the operation of heat pipes in the field of thermal management [21–25]. The difference here is that water transport is driven largely by water saturation gradients, while temperature gradients likely play a secondary role.

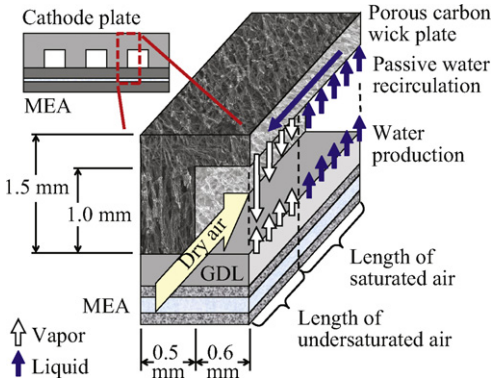

Fig. 1. Schematic of the porous carbon flow field plate and the passive humidification mechanism. Water is produced along the entire channel and is produced in liquid phase towards the end of the channel at sufficiently low air stoichiometric ratios. The porous carbon wick imbibes liquid product water and transports it upstream. At upstream locations, water evaporates from the wick and passively humidifies the air.

In the current study, we experimentally evaluate the merits of using a porous hydrophilic carbon plate with a parallel channel flow field when supplying the fuel cell with dry gases. The analysis compares the fuel cell's performance to that of a fuel cell having a non-porous graphite plate with identical dimensions. The comparison is made using polarization curves and measurements of membrane resistance and air pressure drop. The latter help identify and quantify the effect of flooding and dry-out phenomena.

2. Fuel cell water balance

In this section, we present a theoretical relationship between fuel cell temperature and the air stoichiometric ratio for complete humidification of the gas streams. As the sluggish oxygen reduction reaction is typically the largest irreversibility in the fuel cell, the power density can be significantly improved by operating at the maximum possible temperature because of improved reaction kinetics [11]. In large systems with humidification equipment, the fuel cell temperature is kept below 100 °C because of transitions in Nafion's material properties at higher temperatures [11]. However, when operating with dry gases, the humidification requirement of the membrane determines the maximum feasible temperature rather than material property considerations. If the temperature is too high, the gas streams dry-out the membrane: a result of the exponential relationship between water vapor saturation pressure and temperature. Thus, gas flow rates and temperature must be carefully balanced to maintain sufficient membrane hydration. We can calculate the maximum stoichiometric ratio that permits complete gas saturation at a specified temperature by applying a water mass balance over the fuel cell [11,13]. The mass flow rates of water vapor, $\dot{m}$, into the cathode and anode are

$$\dot{m}_{ca}^{in} = \beta_{ca}^{in} \frac{\alpha_{air}}{0.21} \frac{M_{H_2O} I}{4F} \tag{1}$$

$$\dot{m}_{an}^{in} = \beta_{an}^{in} \alpha_{H_2} \frac{M_{H_2O} I}{2F} \tag{2}$$

where α_{air} and α_{H_2} are the reactant stoichiometric ratios, F is the Faraday constant, and I is the current. The mass flow rates of water vapor in the exhaust gases are:

$$\dot{m}_{ca}^{out} = \beta_{ca}^{out} \left(\frac{\alpha_{air}}{0.21} - 1 \right) \frac{M_{H_2O} I}{4F} \tag{3}$$

$$\dot{m}_{an}^{out} = \beta_{an}^{out} (\alpha_{H_2} - 1) \frac{M_{H_2O} I}{2F} \tag{4}$$

The β parameters in Eqs. (1)–(4) are the water content of the gas flows at the inlets, *in*, and outlets, *out*, of the cathode, *ca*, and anode, *an*, which are expressed as:

$$\beta_{ca,an}^{in,out} = \frac{\varphi_{ca,an}^{in,out} p_{sat}(T_{in,out})}{p - \varphi_{ca,an}^{in,out} p_{sat}(T_{in,out})} \tag{5}$$

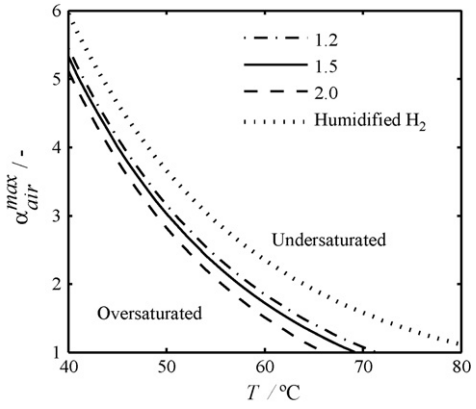

Fig. 2. Maximum air stoichiometric ratio, α_{air}^{max}, for complete saturation of exhaust gases versus fuel cell temperature when inlet gases are dry. Curves for complete humidification are shown for hydrogen stoichiometric ratios of 1.2, 1.5, and 2 and the case of fully humidified hydrogen. Operating points above and to the right of the curves result in undersaturated conditions. Operating points below and to the left of the curves result in saturated gases, indicating the possible presence of liquid water.

where φ is relative humidity, p is the gas pressure, p_{sat} is the vapor saturation pressure, and T is the temperature. From the Faraday relation, we estimate the water production rate of the fuel cell:

$$\dot{m}_{FC} = \frac{M_{H_2O} I}{2F} \tag{6}$$

We can now solve for the maximum air stoichiometric ratio that permits complete humidification of the exhaust gases (assuming steady-state and zero liquid water flow out of the fuel cell): $\varphi_{ca}^{out} = 1$ and $\varphi_{an}^{out} = 1$. To meet this requirement, the mass flow rates of water vapor out of the cell must identically balance the water flow rates into the fuel cell and the water production:

$$\dot{m}_{ca}^{out} + \dot{m}_{an}^{out} - \dot{m}_{ca}^{in} - \dot{m}_{an}^{in} - \dot{m}_{FC} = 0 \tag{7}$$

By substituting Eqs. (1)–(6) into Eq. (7), we can solve for the maximum air stoichiometric ratio for complete humidification:

$$\alpha_{air}^{max} = \frac{0.42[1 + \alpha_{H_2}\beta_{an}^{in} - (\alpha_{H_2} - 1.5)\beta_{an}^{out}]}{\beta_{ca}^{out} - \beta_{ca}^{in}} \tag{8}$$

Fig. 2 shows a plot of the maximum air stoichiometric ratio, α_{air}^{max}, for complete humidification from Eq. (8) as a function of fuel cell temperature for three values of hydrogen stoichiometric ratio when using dry inlet gases. A fourth curve provides α_{air}^{max} for fully humidified hydrogen at for any α_{H_2}. The plots show that the maximum air stoichiometric ratio decreases with increasing temperature. As an illustrative example, we will take the minimum practical stoichiometric ratio as 1.3. In prior work, we identified that an air stoichiometric ratio of 1.3 is roughly the minimum value for stable performance in our cell [9] (lower values cause significant transients and concentration over-voltage). At this air stoichiometric ratio, we see that the maximum possible operating temperature with fully saturated exhaust gases is 65 °C. At lower temperatures, liquid water forms and flooding can occur. We see from the figure that hydrogen stoichiometric ratios have relatively little influence on the maximum temperature due to the low volumetric flow rate of the hydrogen exhaust.

3. Experimental

The fuel cell design and fabrication, as well as the experimental setup are the same as presented in Litster et al. [9]. In this study, there is no active water removal with an electroosmotic pump and we use the wick as a passive water management component. The electroosmotic pump was attached to the wick as in Ref. [9], but no voltage was applied to the EO pump. The EO pump therefore acts as part of the passive wick substrate. The experiments were performed using the same 25 cm^2 active area fuel cell hardware with two versions of a cathode field; one plate is machined from non-porous graphite and the other incorporates a porous carbon plate for wicking. Both flow fields have identical channel and manifold dimensions. The cathode plates have 23 parallel channels which are 1.0 mm deep and 1.2 mm wide. The ribs separating the channels are 1.0 mm wide. Fig. 1 shows the dimensions of the wick. The wick flow field plate is machined from a porous carbon plate (SGL SIGRACET-plate PGP material, SGL Carbon AG, Germany). Heat-treating the plate at 300 °C for 3 min in air makes it hydrophilic. The porous carbon flow field inserts into a machined graphite base for support and edge sealing. For the anode flow field plate, three serpentine channels are machined into a graphite plate. Each channel is 0.75 mm deep and 0.75 mm wide and the rib width is 0.75 mm. The membrane electrode assembly (MEA) features a catalyst coated membrane in which the Nafion membrane is 25 μm thick and the platinum loading is 0.3 mg Pt cm^{-2} (Ion Power, Newcastle, DE). We use SGL-SIGRACET 10-BB (SGL Carbon AG) gas diffusion layers (GDLs).

Table 1
Experimental fuel cell operating conditions.

Parameter	Value
Endplate temperatures (°C)	65
Air and hydrogen inlet dew points (°C)	20 (10% RH)
Gas routing	Counter-flow
Gas line temperatures (°C)	70
Air and hydrogen outlet pressures	Ambient
Hydrogen stoichiometric ratio	1.5

The fuel cell operates in series with a boost power supply (Acopian W3.3MT65, Easton, PA) and a four-wire DC load (Agilent N3100A, Palo Alto, CA). Mass flow controllers (Alicat Scientific, Tucson, AZ) meter the air and hydrogen flow rates. A dew point control system (Bekktech LLC, Loveland, CO) controls the gas dew points, the temperature of the cathode end plate, and the heated lines (Clayborn Labs, Inc., Truckee, CA). A second temperature controller (Omega Engineering Inc., Stamford, CT) maintains constant temperature in the anode endplate. A differential pressure transducer (PX139-030, Omega Engineering Inc.) measures the air pressure drop through the manifolds and channels. The cell resistance is measured with the current interrupt method using the DC load and an algorithm implemented in LabVIEW software. Additional details on the experimental setup and current interrupt method can be found in Ref. [9].

Table 1 presents the fuel cell operating conditions for the proceeding experiments. We chose a hydrogen stoichiometric ratio of 1.5 in all experiments because it enabled continuous operation without flooding in the anode flow field. In these experiments, we ran the fuel cell with end-plate temperatures of 65 °C such that the exhaust gases can become fully saturated when operating with an air stoichiometric ratio of 1.3. During the experiments, we run the gases in a counter-flow orientation for best possible internal water recirculation and humidification with and without integrated wicks. Prior to testing, we condition new MEAs with 10 h of voltage cycling (0.8, 0.5, and 0.3 V for 20 s each).

4. Results and discussion

We now present our experimental analysis of the 25 cm^2 fuel cell when using the non-porous versus porous versions of the parallel channel flow field with dry, ambient pressure gases. First, we examine the transient performance of the two plates and then present

polarization characterization results for the non-porous and porous versions of the parallel channel architecture.

4.1. Transient performance

In this section, we present anecdotal time series of fuel cell voltage and air pressure drop with non-porous and porous plates. The purpose of these results is to convey the fuel cell's improved performance and temporal stability when using the porous plate. To obtain consistent initial conditions, we first operate the fuel cell for 30 min at an air stoichiometric ratio of 2.0 and 0.4 A cm^{-2} current density. We then purge the cathode for 5 s with a high gas flow rate (2 l min^{-1}) before initiating the experiment. During the experiments, the current density increases from 0.1 to 0.3 A cm^{-2} in 0.1 A cm^{-2} increments over 30 min periods. The fuel cell operates with a fixed air stoichiometric ratio of 1.3 because it permits vapor saturated exhaust gases. With Eq. (8), we estimate that stoichiometric ratios greater than 1.4 result in undersaturated gases.

Fig. 3a presents a typical time series of fuel cell voltage and Fig. 3b shows the corresponding time series of air pressure drop. With the non-porous graphite plate, the voltage decays at each increased level of current density. Simultaneous with voltage decay, the air pressure drop increases significantly during the dwells at 0.2 and 0.3 A cm^{-2}. Decreases in voltage and increases in air pressure drop are consistent with flooding and flow maldistribution. This fuel cell is particularly prone to flow maldistribution due to its strictly parallel channel architecture. These results are consistent with observations of severe flooding in previous studies of fuel cell performance with parallel channel flow fields [8,26–28].

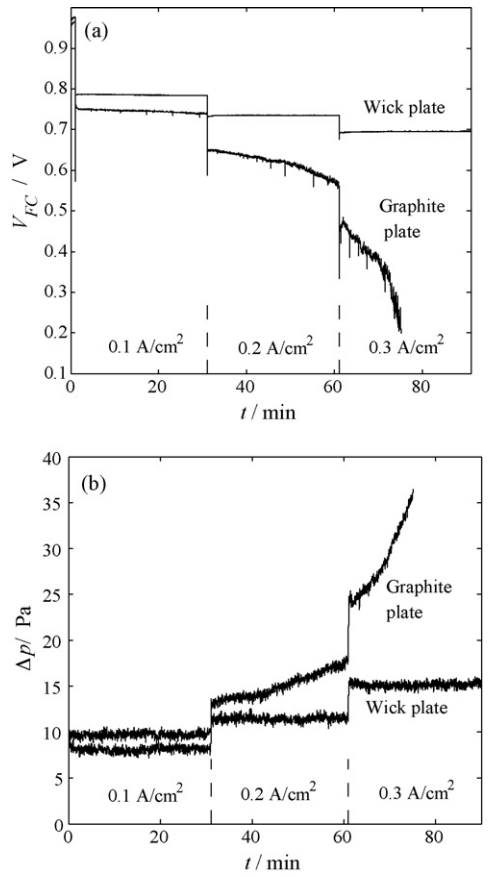

Fig. 3. Time series of fuel cell voltage (a) and air pressure drop (b) at consecutive current densities of 0.1, 0.2, and 0.3 A cm^{-2} for the non-porous graphite plate and the porous carbon wick plate. The current was changed at 1, 31, and 61 min. The fuel cell temperature is 65 °C, the inlet dew points of the air and hydrogen are 20 °C, and the air and hydrogen stoichiometric ratios are 1.3 and 1.5, respectively.

In contrast to the results of the non-porous plate, the voltage time series for the porous plate is invariant in time at each level of current density shown in Fig. 3a. This voltage time series correlates well with the steady air pressure differential at each current density. The step function form of the voltage and air pressure drop time series demonstrates that water redistribution within the porous plate reduces both water accumulation in the channels and the deleterious effects of flooding. Using passive wicking to prevent flooding results in significant increases in fuel cell voltage. Furthermore, the temporal stability of fuel cell performance is drastically improved with the porous plate.

4.2. Polarization with non-porous plates

We now examine the polarization results of the fuel cell with the non-porous plate at air stoichiometric ratios ranging from 1.3 to 3. The polarization data include measurements of voltage, membrane resistance, and air pressure drop. These results serve as a control case to which we will compare the porous plate system performance.

The period of time that each polarization point is held has a significant impact on the data measured when using under-humidified gases [12]. Hogarth and Benziger [29] reported that their equilibration times with dry gases were commonly 1–4 h and in some cases required a 24 h period. Previous studies with under-humidified gases often used shorter periods or did not report equilibration times. For example, Williams et al. [10] and Vengatesan et al. [30] measured polarization curves with dry gases using dwell periods of 5 min. The data points presented here are the time mean values from the last 4 min of a 30 min dwell at each current density. We note that a 30 min dwell is not necessarily sufficient to reach steady-state in all conditions, but it provides well-controlled, representative values for comparisons between the two plates studied. Before the measurement of each polarization curve, we established the fuel cell's initial state using the same procedure used for the transient measurements in the previous section. The polarization curve measurements were terminated when the instantaneous fuel cell voltage fell below 0.2 V.

Fig. 4a presents the polarization curves of the fuel cell with the non-porous plate. We identify two significant trends associated with this combination of dry gases and high plurality of parallel channels in a non-porous plate. First, we observed that the maximum current density increased with greater air stoichiometric ratios up to a value of 1.8. However, air stoichiometric ratios above 1.8 resulted in decreased maximum current densities. Second, we observed an unusual concave up curvature in the polarization curves, particularly at air stoichiometric ratios of 1.8 and 2. Fig. 4b presents the IR-free form of the polarization curves in which we have subtracted the Ohmic overpotential (measured with the current interrupt method). The upward concavity is more pronounced for the IR-free polarization curves. Thus, we attribute this curvature to mass transfer limitations rather than membrane resistance. We note that the time series of voltage displayed both instabilities and transitions requiring more than 30 min to equilibrate over the majority of 1.5–4 h polarization curve measurement periods.

Fig. 4c presents the membrane resistance for the non-porous plate polarization. The membrane resistance is the total resistance subtracted by the electric resistance (resistance of the plates and GDLs). The electric resistance estimate is the difference between the fully humidified membrane resistance measured by Sone et al. [31] and the total resistance when we operate the fuel cell with fully humidified gases. The estimated electric resistances of the fuel cell with non-porous and porous plates are 0.069 and 0.106 Ω cm^2, respectively. The higher electric resistance with the porous plate

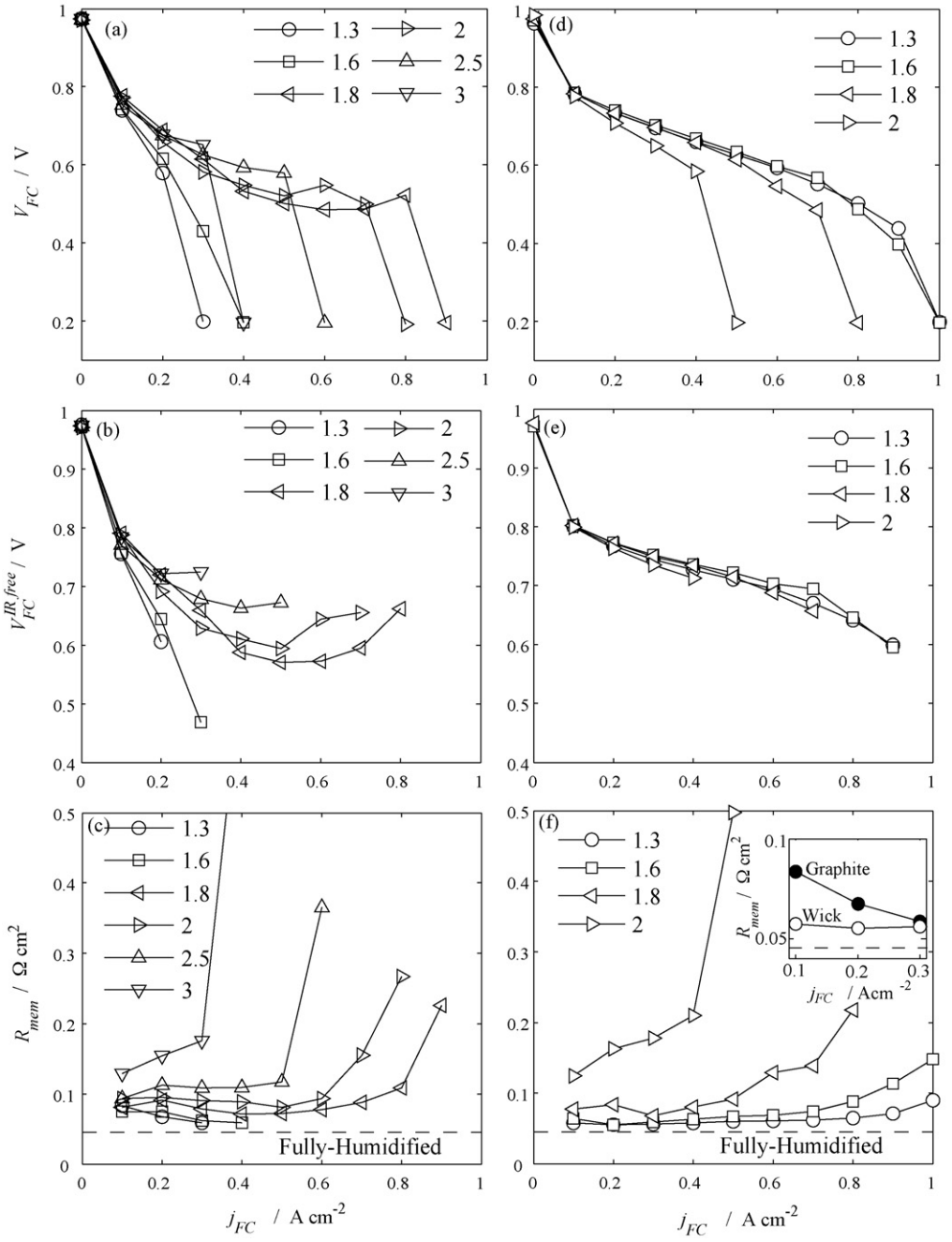

Fig. 4. Data comparing non-porous and porous plate fuel cells. Polarization curves (a), IR-free polarization curves (b), and membrane resistance curves (c) for the fuel cell with a non-porous graphite plate. Polarization curves (d), IR-free polarization curves (e), and membrane resistance curves (f) for the fuel cell with the porous hydrophilic carbon plate. The dashed lines in (c) and (f) are the estimated resistance of a fully humidified membrane. The inset plot in (f) is a comparison between the membrane resistance between the two plates at α_{air} = 1.3 ("graphite" and "wick" are respectively the non-porous and porous plates).

is due to its porosity and the contact resistance of the additional interface between the porous plate and the non-porous graphite base [9].

At the lower air stoichiometric ratios and current densities, the membrane resistance of the fuel cell with the non-porous plate decreased with increasing current density. This occurs because increasing water production rate increases the humidification of the membrane at these operating conditions [10]. In contrast, at high air stoichiometric ratios and high current densities, the membrane resistance significantly increased as the membrane dried. These trends in membrane resistance are consistent with those reported in the literature, such as those by Williams et al. [10]. At air stoichiometric ratios of 1.8 and higher, the large increases in membrane resistance at the maximum current density indicate that membrane dry-out limited the maximum current rather than mass transport limitations. The membrane dry-out is likely accelerated at the limiting current density by increased internal heating in the MEA [12,32].

Fig. 5 presents the non-porous plate's air pressure drop measurements normalized by the air stoichiometric ratio. We normalize the air pressure drop to distinguish changes in the hydraulic resistance at six air stoichiometric ratios. The air pressure drops are significantly lower than typical (<100 Pa versus 1–10 kPa [33]) because of the parallel channel flow field's low hydraulic resistance. The normalized air pressure drops are highest at the lower air stoichiometric ratios of 1.3 and 1.6 and increase sharply at the maximum

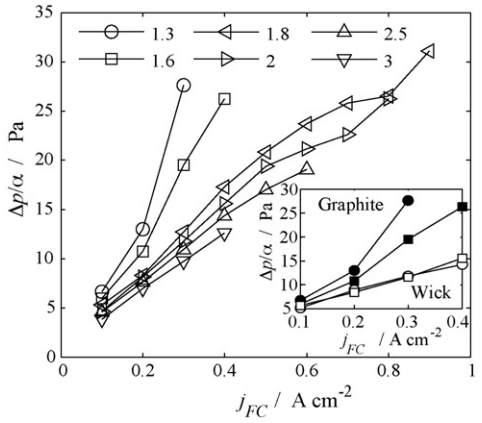

Fig. 5. Air pressure drop measurements with the non-porous graphite plate for air stoichiometric ratios of 1.3, 1.6, 1.8, 2, 2.5 and 3. The pressure drops are normalized by the air stoichiometric ratio. At low air stoichiometric ratios, liquid water accumulates, causing increased pressure drops and flooding. The inset compares normalized air pressure drops between the graphite (non-porous) and wick (porous) plates at stoichiometric ratios of 1.3 and 1.6 (see legend in main figure).

current density. High values of the normalized air pressure drop are consistent with liquid water accumulation [27]. In Fig. 5, increasing and decreasing slope in the curves of air pressure drop indicate liquid water accumulation and removal with increases in current density, respectively. Thus, the decreasing slopes at moderate to high current densities in Fig. 5 at air stoichiometric ratios of 1.8 and greater indicate the removal of liquid water from the channels.

From the resistance and pressure drop results, we infer that the unusual concave up curvature in the polarization curves and IR-free polarization curves (cf. Fig. 4) arise due to flooding at low to mid-current densities and dry-out at high current densities. This low current density flooding with dry gases is specific to our use of parallel channels. Water will likely accumulate unevenly amongst parallel channels, and so flow maldistribution arises since channels containing less liquid water support a greater portion of the total gas flow. The maldistribution causes some channels to have a relatively high stoichiometric ratio and others to have a relatively low stoichiometric ratio (relative to the system-wide value). Thus, the fuel cell with a non-porous plate with parallel channels consistently suffers from dry-out, flooding, or a state where both phenomena occur simultaneously in distinct zones. Overall, this polarization characterization and the transient data in the previous section demonstrate that the combination of dry gases and parallel channels results in unacceptable performance when using a traditional non-porous plate.

4.3. Polarization with porous plates

We now present the polarization characterization of the fuel cell with a porous plate, and compare these to the control case of the non-porous plate. The porous plate has the same macroscopic flow field geometry and dimensions as the non-porous plate. The polarization characterization of this fuel cell was performed at air stoichiometric ratios of 1.3, 1.6, 1.8, and 2.

The (porous plate design) polarization curves in Fig. 4d show that we obtained high performance with air stoichiometric ratios of 1.3 and 1.6. At low to moderate current densities (<0.8 A cm^{-2}), an air stoichiometric ratio of 1.6 provides the highest voltages. At higher current densities, we obtained the highest voltages with an air stoichiometric ratio of 1.3. With the IR-free polarization curves in Fig. 4e, we determine that the slightly higher voltages at low current densities at an air stoichiometric ratio of 1.6 are attributable to higher oxygen concentration near the outlet. In contrast, at high current densities we measured higher voltages with an air stoichiometric ratio of 1.3 because of lower membrane resistance (see Fig. 4f). Further, the membrane resistance is near its minimum level (completely hydrated) over a wide range of current densities at an air stoichiometric ratio of 1.3. The lower voltages in the porous plate's polarization curves at higher air stoichiometric ratios of 1.8 and 2 are due to high membrane resistance (i.e., dry-out with undersaturated gases). In comparison to the non-porous plate, the porous plate offers significantly improved membrane hydration at an air stoichiometric ratio of 1.3 (see the inset of Fig. 4f).

We verify flood prevention with the porous plate using both IR-free polarization curves and air pressure drop measurements. With the porous plate, we see that IR-free polarization curves (Fig. 4e) are independent of air stoichiometric ratio relative to the non-porous plate's curves (Fig. 4b). The comparison of air pressure drop measurements between the porous and non-porous plates (inset of Fig. 5) depicts significantly less resistance to air flow through the channels. Thus, it is evident that there is significantly less water accumulation and flooding in the porous plate's channels.

The polarization curves of the fuel cell with the porous plate show the significantly improved power density in comparison to the non-porous plate. With the porous plate, the highest maximum power density we obtained was 0.40 W cm^{-2} (air stoichiometric ratio of 1.3). This power density is 3.5 times greater than the maximum achieved with the non-porous plate at the same air stoichiometric ratio. For short periods, the non-porous plate can provide similar maximum power density at higher stoichiometric ratios. However, as we note above, the non-porous plate's performance is unstable at the majority of the operating conditions we explored. With the porous plate, the voltage is stable up to a current density of 0.7 A cm^{-2} at an air stoichiometric ratio of 1.3. At current densities greater than 0.7 A cm^{-2}, we observe voltage (temporal) fluctuations attributable to flooding, which we have shown can be mitigated by coupling the wick with an active water removal using an EO pump [9].

We credit the better performance of the porous plate design to passive water redistribution and internal air humidification. These mechanisms act in concert to both reduce flooding and increase membrane hydration. In this scenario, capillary flow (wicking) drives liquid water from saturated zones to regions where the air is undersaturated. In these regions, the liquid water in the porous plate evaporates into the gas stream. Our measurements of polarization, air pressure drop, and membrane resistance strongly support this hypothesis. The fact that the porous plates reduce susceptibility to flooding by wicking dynamics is supported by the nearly noise free (low fluctuation) time series of air pressure drop (see Fig. 3b for example), and the low sensitivity of the IR-free polarization curves to the air stoichiometric ratio. Passive internal humidification is evidenced by the 45% increase in membrane conductivity at the lowest current density (0.1 A cm^{-2}) when using the air stoichiometric ratio that permits saturated air (α_{air} = 1.3). Clearly, this combination of stability and power density with parallel channels and dry gases is not possible with the non-porous graphite plate.

5. Conclusion

In this work, we have evaluated the performance of PEM fuel cells having parallel channels and operating on dry, ambient pressure gases. Our results include an experimental comparison between a hydrophilic, porous carbon cathode plate and a non-porous graphite plate with the same dimensions. Polarization curves and pressure and resistance measurements demonstrate the challenges associated with using a non-porous plate, which include simultaneous flooding and dry-out. In contrast, the porous carbon plate provides significantly improved performance and stability.

For the latter case, we obtain a stable maximum power density of 0.4 W cm^{-2} using an air stoichiometric ratio of 1.3; a power density that is 3.5 times greater than that delivered by the non-porous plate at the same condition.

We presented a hypothesis that the porous plate removes excess liquid from downstream locations to prevent flooding and redistributes the water upstream for humidification via capillary forces. Because of passive water redistribution, the fuel cell does not flood at low air stoichiometric ratios and the membrane conductivity is near its maximum, fully hydrated level. Thus, the porous carbon design has the potential to enable a fuel cell system with a minimum balance of plant components and a low air delivery parasitic load. This combination of design properties and performance figures of merit makes this implementation of passive wicking especially applicable to fuel cells for portable power applications which have open-ended parallel channels and high requirements for volumetric power density and system simplicity.

Acknowledgement

The authors acknowledge a Post-Graduate Scholarship from the Natural Science and Engineering Research Council of Canada for S. Litster.

References

[1] National Hydrogen Energy Roadmap, US Dept. of Energy, 2002.
[2] R.K. Ahluwalia, X. Wang, A. Rousseau, R. Kumar, J. Power Sources 130 (2004) 192–201.
[3] F. Urbani, G. Squadrito, O. Barbera, G. Giacoppo, E. Passalacqua, O. Zerbinati, J. Power Sources 169 (2007) 334–337.
[4] D.T. Santa Rosa, D.G. Pinto, V.S. Silva, R.A. Silva, C.M. Rangel, Int. J. Hydrogen Energy 32 (2007) 4350–4357.
[5] M. Oszcipok, M. Zedda, J. Hesselmann, M. Huppmann, M. Wodrich, M. Junghardt, C. Hebling, J. Power Sources 157 (2006) 666–673.
[6] A. Heinzel, C. Hebling, M. Müller, M. Zedda, C. Müller, J. Power Sources 105 (2002) 250–255.
[7] Y. Tabe, S.K. Park, K. Kikuta, T. Chikahisa, Y. Hishinuma, J. Power Sources 162 (2006) 58–65.
[8] W.R. Mérida, G. McLean, N. Djilali, J. Power Sources 102 (2001) 178–185.
[9] S. Litster, C.R. Buie, T. Fabian, J.K. Eaton, J.G. Santiago, J. Electrochem. Soc. 154 (2007) B1049–B1058.
[10] M.V. Williams, H.R. Kunz, J.M. Fenton, J. Power Sources 135 (2004) 122–134.
[11] F. Barbir, PEM Fuel Cells: Theory and Practice, Elsevier Academic Press, London, 2005.
[12] T. Fabian, J.D. Posner, R. O'Hayre, S.W. Cha, J.K. Eaton, F.B. Prinz, J.G. Santiago, J. Power Sources 161 (2006) 168–182.
[13] F.N. Büchi, S. Srinivasan, J. Electrochem. Soc. 144 (1997) 2767–2772.
[14] Z. Qi, A. Kaufman, J. Power Sources 109 (2002) 469–476.
[15] M. Watanabe, H. Uchida, Y. Seki, M. Emori, P. Stonehart, J. Electrochem. Soc. 143 (1996) 3847–3852.
[16] J.S. Yi, J.D.L. Yang, C. King, AIChE J. 50 (2004) 2594–2603.
[17] J.P. Meyers, R.M. Darling, C. Evans, R. Balliet, M.L. Perry, ECS Trans. 3 (2006) 1207–1214.
[18] S.H. Ge, X.G. Li, I.M. Hsing, Electrochim. Acta 50 (2005) 1909–1916.
[19] S.H. Ge, X.G. Li, I.M. Hsing, J. Electrochem. Soc. 151 (2004) B523–B528.
[20] D.G. Strickland, S. Litster, J.G. Santiago, J. Power Sources 174 (2007) 272–281.
[21] K.S. Udell, Int. J. Heat Mass Transfer 28 (1985) 485–495.
[22] J. Rice, A. Faghri, J. Thermophys. Heat Transfer 21 (2007) 475–486.
[23] A. Nouri-Borujerdi, M. Layeghi, J. Porous Media 8 (2005) 471–480.
[24] B.K. Tan, X.Y. Huang, T.N. Wong, K.T. Ooi, Int. J. Heat Mass Transfer 43 (2000) 3755–3764.
[25] A. Faghri, M. Buchko, J. Heat Transfer 113 (1991) 728–734.
[26] X. Liu, H. Guo, C. Ma, J. Power Sources 156 (2006) 267–280.
[27] X. Liu, H. Guo, F. Ye, C.F. Ma, Electrochim. Acta 52 (2007) 3607–3614.
[28] T.V. Nguyen, J. Electrochem. Soc. 143 (1996) L103–L105.
[29] W.H.J. Hogarth, J.B. Benziger, J. Power Sources 159 (2006) 968–978.
[30] S. Vengatesan, H.J. Kim, E.A. Cho, S.U. Jeong, H.Y. Ha, I.H. Oh, S.A. Hong, T.H. Lim, J. Power Sources 156 (2006) 294–299.
[31] Y. Sone, P. Ekdunge, D. Simonsson, J. Electrochem. Soc. 143 (1996) 1254–1259.
[32] S. Litster, N. Djilali, Electrochim. Acta 52 (2007) 3849–3862.
[33] F. Barbir, H. Gorgun, X. Wang, J. Power Sources 141 (2005) 96–101.